PAPER

Germanium coating boosts lithium uptake in Si nanotube battery anodes†

Marta Haro,‡[a] Taeseup Song,‡[b] Antonio Guerrero,[a] Luca Bertoluzzi,[a] Juan Bisquert,[a] Ungyu Paik*[b] and Germà Garcia-Belmonte*[a]

Si nanotubes for reversible alloying reaction with lithium are able to accommodate large volume changes and offer improved cycle retention and reliable response when incorporated into battery anodes. However, Si nanotube electrodes exhibit poor rate capability because of their inherently low electron conductivity and Li ion diffusivity. Si/Ge double-layered nanotube electrodes show promise to improve structural stability and electrochemical kinetics, as compared to homogeneous Si nanotube arrays. The mechanism explaining the enhancement in the rate capabilities is revealed here by means of electrochemical impedance methods. The Ge shell efficiently provides electrons to the active materials, which increase the semiconductor conductivity thereby assisting Li^+ ion incorporation. The charge transfer resistance which accounts for the interfacial Li^+ ion intake from the electrolyte is reduced by two orders of magnitude, indicating the key role of the Ge layer as an electron supplier. Other resistive processes hindering the electrode charge–discharge process are observed to show comparable values for Si and Si/Ge array electrodes.

Introduction

Among various alloying-type anode materials for lithium ion batteries (LIB), Si has received considerable attention due to its highest theoretical capacity, 4200 mA h g^{-1} at the fully lithiated state $Li_{22}Si_5$, being the most promising alternative to carbon anodes.[1,2] Although the fast capacity fading of Si electrodes (resulting from a large volume change associated with lithium ions) has been considered as a main obstacle for their practical use, significant improvement in the cycle performance has been achieved by engineering the geometry and dimension of Si anode materials.[3,4] Especially, Si nanotube (Si NT) arrays exhibited robust cyclability due to the reversible morphological change.[5–7] Electrode materials for LIB should be designed to fulfill both energy density and power density requirements of critical applications such as large-scale storage for renewable power sources, electric vehicles, and plug-in hybrid electric vehicles. However, Si NT electrodes could not meet the demand for the high power density due to their poor rate capability attributed to inherently low electron conductivity and ion diffusivity. To improve these two parameters researchers have

investigated in the last few years different strategies such as the growth of Si on nanopillar metallic structures,[8] fabrication of core–shell composites,[9] or coating of Si electrodes with a good electron and/or ion conductor (polymer, graphene, *etc.*).[10–14] Very recently, Si/Ge double-layered nanotube (Si/Ge DLNT) arrays prepared by employing a template-assisted synthesis method based on a chemical vapor deposition process have been reported.[15] With optimal designs, Si/Ge DLNTs exhibited significant improvements in structural stability and electrochemical kinetics in comparison to homogeneous Si NTs. Although it is evident that high electronic conductivity and ionic diffusivity in Ge in comparison to Si aid to explain the kinetic improvements, the exact mechanism (either electronic conduction, ionic migration, charge transfer, or alloying reaction) that lies behind such an enhancement is still unclear.[15–17]

We conclude by means of impedance spectroscopy measurements that the incorporation of Li-ions from the electrolyte into the semiconductor structures is highly favored by the Ge shell covering inner Si nanotubes. This is principally related to the higher electronic conductivity that Ge possesses in comparison to Si. The analysis of the resistive processes hindering the electrode charging points to a kinetic limitation in the case of Si NTs related to interfacial mechanisms. The total resistance for Si NT electrodes doubles that encountered for Si/Ge DLNT structure in the range of the alloying reaction potentials. The rate capability is then enhanced by incorporating the Ge shell that reduces the charge transfer resistance associated with the Li-ion intake.

[a] Photovoltaics and Optoelectronic Devices Group, Departament de Física, Universitat Jaume I, 12071 Castelló, Spain. E-mail: garciag@fca.uji.es

[b] Department of Energy Engineering, Hanyang University, Seoul 133-791, Korea. E-mail: upaik@hanyang.ac.kr

1. Results and discussion

1.1. Electrochemical properties

Experimental details of the synthesis and evaluation of electrochemical properties of both the Si NT and the Si/Ge DLNT anodes have been fully addressed in previous reports.[7,15] Fig. 1a and b display low magnification transmission electron microscopy (TEM) images of a SiNT and a Si/Ge DLNT. Both the Si NT and Si/Ge DLNT show tubular morphology and identical dimensions. The Si NT has the outer diameter of ~120 nm and a shell thickness of ~30 nm. In the Si/Ge DLNT, a Ge shell layer with a thickness ranging from 10 to 15 nm is uniformly coated on the surface of a SiNT with a thickness ranging from 15 to 20 nm and the inner diameter of ~60 nm.

The electrochemical performances of both Si NT and Si/Ge DLNT electrodes were evaluated over the potential window of 0–2.0 V *vs.* Li/Li$^+$ at room temperature (25 °C). Fig. 1c shows the voltage profiles at the first cycle for Si NT and Si/Ge DLNT electrodes. Although the Si NT electrode (~2650 mA h g^{-1}) delivered ~2-fold higher gravimetric capacity than that of the Si/Ge DLNT electrode (~1550 mA h g^{-1}), the Si/Ge DLNT electrode (~1.2 mA h cm^{-2}) exhibited 2-fold higher areal capacity compared to that of the SiNT electrode (~0.6 mA h cm^{-2}) along with improved cycle performance. Ge has 2.3 times higher specific density (5.323 g cm^{-3}) compared to that of Si (2.329 g cm^{-3}), which leads to the higher areal energy density in the Si/Ge DLNT electrode. The Si NT and Si/Ge DLNT electrodes showed totally different voltage profiles during lithiation. The Si NT electrode shows a long plateau near 0.1 V, which corresponds to the alloying reaction of the crystalline Si with lithium. The Si/Ge DLNT array showed two distinct voltage plateaus in the discharge voltage profile. The first voltage plateau, located between 0.2 and 0.4 V, and the second downward slope voltage plateau, located under 0.2 V, are attributed to the alloying reactions of the Ge shell layer and Ge/Si with lithium, respectively. In previous study, we explored the cycle performances of both the Si NT and Si/Ge DLNT electrodes. The Si NT and Si/Ge NT electrodes exhibited cycle performances of 82% and 85% at 0.2 C rate after 50 cycles, respectively.[7,15] The rate capability of Si NT and Si/Ge DLNT electrodes was carefully evaluated at various C-rates (Fig. 1d). The Si/Ge DLNT electrode exhibits significantly improved rate capability compared to that of the Si NT electrode. While the Si/Ge DLNT electrode retains the capacity over 60% at a 3 C rate, the Si NT electrode delivers very low capacity (35%). This significant improvement in rate capability observed for the Si/Ge DLNT might be related to several steps involved in the lithiation–delithiation process. To further understand the kinetics of Li-ion intake and the subsequent alloying reaction anodes are investigated by using electrochemical impedance spectroscopy (EIS) methods.

1.2 Impedance responses

Kinetic of the charging–discharging process have been addressed by analyzing EIS response performed at quasi steady-state (no direct current flow) at different charge states between 0 V and 1.2 V, with an ac amplitude of 20 mV in the frequency range from 10^6 Hz down to 0.001 Hz. Kinetic limitations can be easily inferred
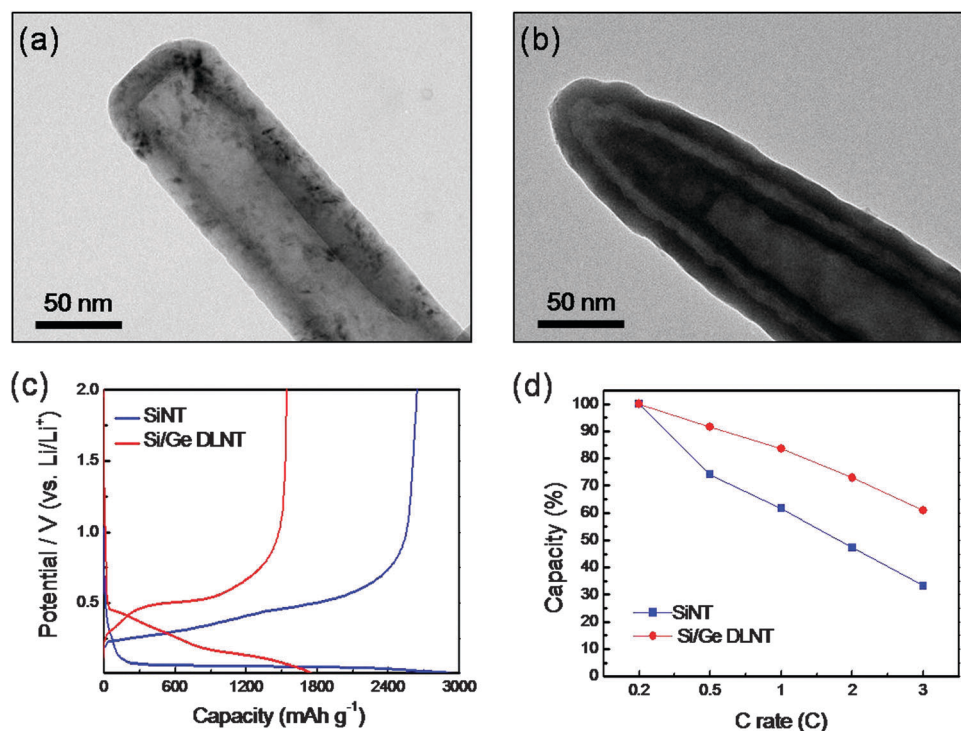

Fig. 1 TEM images of a SiNT (a) and a Si/Ge DLNT (b). The first voltage profiles at a rate of 0.2 C (c) and rate capabilities (d) for SiNT and Si/Ge DLNT electrodes.
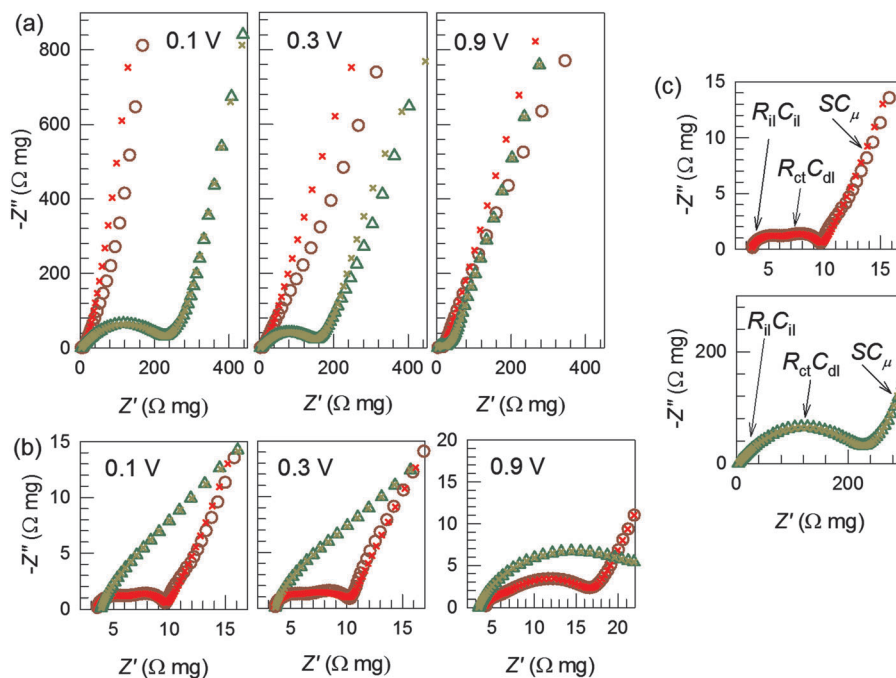
Fig. 2 Impedance spectroscopy response of Si NT (triangle) and Si/Ge DLNT (circle) electrodes at different steady-state voltages as indicated. (a) A complete view showing a low-frequency capacitive-like response. (b) High-frequency detail with the interfacial behavior. Experimental data and fits (cross) using the equivalent circuit Fig. 3a. (c) Impedance patterns at 0.1 V in relation to the equivalent circuit elements of Fig. 3a.

from resistive processes occurring during the electrode operation under steady-state conditions. All the results are normalized by the weight for a clearer comparison. Representative Nyquist plots are represented in Fig. 2, which consist of two well-defined parts: the high-frequency semicircles and an inclined low-frequency capacitive-like line. At high frequencies, a rather constant, minor arc corresponds to the parallel connection between the interlayer capacitance $C_{il} \approx$ 2–70 µF mg^{-1} and migration resistance $R_{il} \approx$ 2–10 Ω mg (Fig. 2b). This resistive contribution is usually caused by the Li migration through external layers as those formed by the solid electrolyte interface (SEI) associated with the electrolyte decomposition (see Fig. 3a). This impedance contribution is significantly smaller than the additional arc observed at intermediate-frequencies, clearly visible in the case of Si NT electrodes, which is interpreted in terms of the mechanisms occurring at the electrical double-layer formed at the nanotubes (Fig. 3a). The intermediate process is modeled by means of double-layer capacitance C_{dl} and charge transfer resistance R_{ct}. The charge transfer resistance is related to the Li-ion intake step of the nanotubes. A huge difference is observed in the charge transfer resistance R_{ct} corresponding to the intermediate arc when Si and Si/Ge-based electrodes are compared. While Si NT electrodes exhibit an increase in R_{ct} when the potential is reduced below 0.5 V ($R_{ct} \approx$ 200 Ω mg), the incorporation of a Ge layer reduces the charge transfer resistance to values as low as $R_{ct} \approx$ 3 Ω mg as observed in Fig. 2b. The porosity of the electrodes yields double-layer capacitance values in the order of $C_{dl} \approx$ 10 µF mg^{-1}. A connection between the impedance patterns and the corresponding circuit elements (Fig. 3a) can be viewed in Fig. 2c. This equivalent circuit accounts for the high-frequency impedance
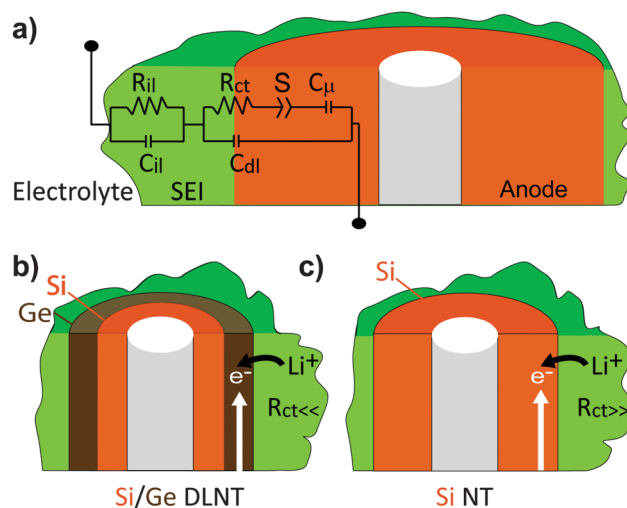

Fig. 3 (a) Schematic view of the relationship between equivalent circuit elements and electrode layers. R_{il} and C_{il} account for high-frequency processes occurring at the outer SEI layer. Interfacial mechanisms are modeled with R_{ct} and C_{dl} circuit elements. In series with R_{ct} the alloying reaction subcircuit includes the elements S and C_{μ}. (b) Favored electron conduction through the Ge shell assists the Li-ion intake reducing R_{ct}. (c) Difficult conduction in the Si layer yields large values for R_{ct}.

response with the parameters R_{il}, R_{ct}, C_{il}, and C_{dl}. A small series resistance accounts for the solution contribution (not shown in Fig. 3a).

The high-frequency circuit elements are observed to change at potentials approaching alloying reactions, then signaling that mechanisms occurring at the interface are influenced by

17932 | *Phys. Chem. Chem. Phys.*, 2014, **16**, 17930–17935

This journal is © the Owner Societies 2014

the electrode state of charge. It is worth noting here that the resistive parameter that exhibits the main difference between Si NT and Si/Ge DLNT electrodes is the charge transfer resistance R_{ct}, which is reduced by more than two orders of magnitude. This resistance is connected to the Li intake from the solution to the semiconductor layer as schematically displayed in Fig. 3b and c. The Ge shell allows for an enhanced electron path facilitating the Li-ion intake at the semiconductor interface. It has been observed for other insertion compounds that R_{ct} is directly related to the electronic conductivity of the host material.[18] Highly conductive hosts permit the Li ion to overcome the potential barrier appearing at the solution/semiconductor interface. In the case under study it is known that Ge electronic conductivity exceeds by four orders of magnitude that encountered for Si. This fact explains the observed reduction in R_{ct} for potentials in the alloying reaction range. Alternatively, the intermediate arc resistance might also be directly related to the electronic conductivity of the semiconductor. But in this last case it is hard to understand how R_{ct} presents values in the range of 100–200 Ω mg for both electrodes at potentials in excess of 0.5 V (see Fig. 2b). This fact leads us to connect the limiting lithiation mechanism represented by R_{ct} to the process of Li-ion incorporation into the semiconductor matrix.

Quality of the fits was checked by analyzing confidence intervals and correlation between parameters as a discriminating tool for stating the best set of fitting parameters. Confidence levels are always high enough ($>99\%$) to consider the parameter values a very good estimation of the model quantities. In all cases the regression coefficient of fits $r^2 > 0.997$. The combination of these statistics (namely, dependencies between parameters, confidence levels, and regression coefficients) signals the high accuracy that can be reached using the simple model of Fig. 3a. Nonetheless, fits deviate from data for some spectra in the low-frequency range (see Fig. 2a), where the response is basically capacitive. However, the quality of the fits is good in the high- and intermediate-frequency range as observed in Fig. 2c. It is precisely in these frequency regions that the principal resistive mechanisms are visible. For this reason we consider the fit good enough for our purposes of quantifying resistive limitations. Parameter values drawn in Fig. 4a–d result from fitting the equivalent circuit to the experimental impedance data. It is especially interesting to note the behavior exhibited by the charge transfer resistance (Fig. 4d) as it corresponds to the main hindrance mechanism for Li-ion supply to the alloying compound. For potentials below 0.5 V, Si NT arrays undergo an increase in R_{ct} of one order of magnitude (from $\sim$20 Ω mg up to $\sim$200 Ω mg). In contrast Si/Ge DLNTs exhibit the expected variation: as the system reaches the alloying potentials Ge conductivity is enhanced then reducing R_{ct}. We can conjecture that this dissimilar behavior might be related to the different doping character of Si and Ge layers, although more investigations are needed on this concern that lies outside the scope of this work.

The low-frequency EIS response points to the occurrence of a voltage-modulated process which gives rise to a capacitive-like behavior. This behavior is connected to the so-called chemical capacitance that results from the ability of electrodes to vary the
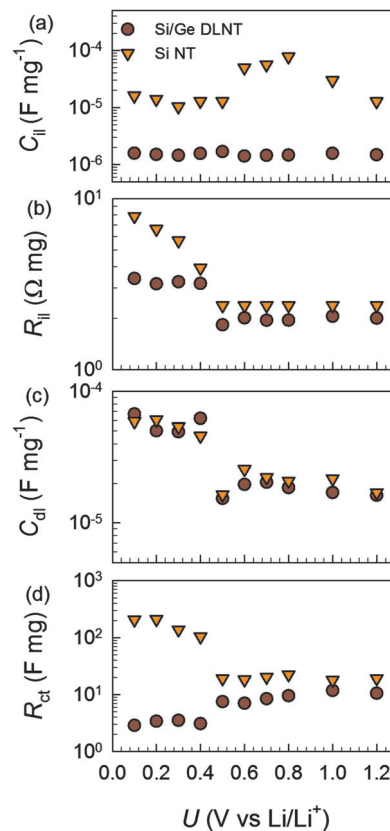

Fig. 4 Fitting results using the equivalent circuit of Fig. 3(a) for the high-frequency circuit elements of Si and Si/Ge NT anodes showing (a) inter-layer capacitance C_{il} and (b) migration resistance R_{il}. (c) Double-layer capacitance C_{dl} and (d) charge transfer resistance R_{ct}.

amount c of reacted Li$^+$ upon application of a differential change in the chemical potential μ (directly assimilated to the electrode potential under steady-state conditions as $\mu = qU$, where q is the positive elementary charge).[19] The chemical capacitance can be written as

$$C_\mu = q\frac{dc}{dU} \qquad (1)$$

Accompanying the chemical capacitance at low-frequencies it is observed that a concomitant increase in the real part of the impedance appears to be added to the previous resistances acting at higher-frequencies (Fig. 2a). It is noticeable that this extra resistance at low-frequencies R_a exhibits similar values for Si NT and Si/Ge DLNT electrodes. As previously commented, resistances in the equivalent circuit signal the occurrence of different rate-limiting mechanisms. For intercalation compounds the diffusion of Li$^+$ inside the host material is one of the rate-limiting processes.[20] Diffusion of ions gives rise to distinctive impedance patterns characterized by Warburg-like responses as $Z \propto (i\omega)^{-1/2}$ (ω being the angular frequency and $i = \sqrt{-1}$). Previous models based on spatially-restricted ion diffusion were proposed relying on a distribution of diffusion lengths[21] or electronic transport limitations.[22] However, Si NT and Si/Ge DLNT electrodes function by alloying reactions

This journal is © the Owner Societies 2014

Phys. Chem. Chem. Phys., 2014, **16**, 17930–17935 | 17933

yielding a complete chemical and structural electrode material rearrangement. The fact that no Warburg-like pattern is observed in the low-frequency response in Fig. 2a leads us to regard the alloying reaction itself as the origin for the additional resistance at low frequencies. The resistive process R_a accompanying the chemical capacitance is seen then as a contribution to the alloying-related current hindrance.[23]

The coupling between chemical capacitance C_μ and reaction resistance R_a has been addressed in previous studies.[24] In terms of equivalent circuits the alloying reaction can be modeled by means of a series connection of C_μ and a suitable generalization of R_a (a constant phase element CPE with impedance $Z_{CPE} = 1/S(i\omega)^\alpha$) as drawn in the equivalent circuit of Fig. 3a. The effective alloying resistance can be calculated from fitting parameters by means of the next expression,[24]

$$R_a = (C_\mu^\alpha/S)^{\frac{1}{1-\alpha}} \qquad (2)$$

here S accounts for the CPE parameter and α informs on the broadening in the reaction rate distribution. Fig. 5 summarizes the fitting results. It is observed in Fig. 5a that the chemical capacitance C_μ steeply increases toward low potentials. C_μ values are obtained in the order of 0.1 F mg^{-1} at low voltages for both electrodes informing about the similar alloying ability of both Si and Si/Ge semiconductors. It is interesting to point out that the chemical capacitance correlates with the discharge curve derivative $-dQ/dU$. Recalling Fig. 1c now, long plateaus are observed for both electrodes at low voltages. This is in good agreement with the C_μ maxima at 0.1 V.

The parameter accounting for the electrochemical kinetics is the alloying resistance of eqn (2). One can infer from Fig. 5b that R_a exhibits similar values for both Si NT and Si/Ge DLNT electrodes at low potentials. It is known that specific capacity at different C-rates can also be analyzed in terms of the resistive mechanisms accompanying the charging–discharging process. As shown in Fig. 1d, a noticeable capacity decrease for the Si NT electrode was observed at 0.5 C. This is caused by a significant
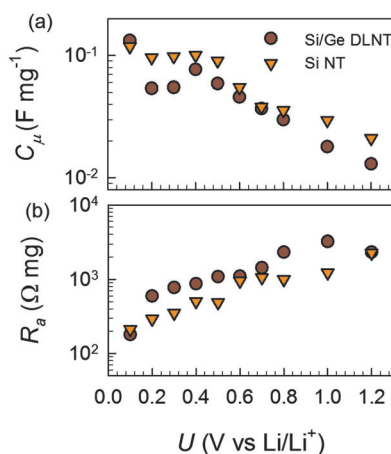
increase in the total resistance that at 0.1 V approximately amounts to 200 Ω mg for Si/Ge DLNT electrodes, while that value doubles (400 Ω mg) in the case of Si NTs. For higher charging–discharging rates high-frequency resistances $R_{il} + R_{ct}$ take the control of the kinetic response. In this case the difference between the resistive response of Si NTs (270 Ω mg) and Si/Ge DLNTs (50 Ω mg) is even larger. We remark again that the main contribution for increasing the Li-ion intake hindrance is caused by the superior charge transfer resistance exhibited by Si NT electrodes. This last observation clarifies the origin of the difference in the rate capability.

With the aim of further illustrating the detrimental effect of resistive elements on the C-rate performance, we have reproduced a simplified version of the discharge curve based on the equivalent circuit in Fig. 3a. In order to assess the relative importance of the extraction current, I_0, and charge transfer resistance, R_{ct}, in the voltage decay, the electrode has been modeled by using the electrical circuit of Fig. 6a. This circuit only takes into account the largest capacitive contribution. For the sake of simplicity, chemical capacitance has been selected as a constant, while R_a follows the decreasing behavior with voltage shown in Fig. 5b. The total specific charge in each
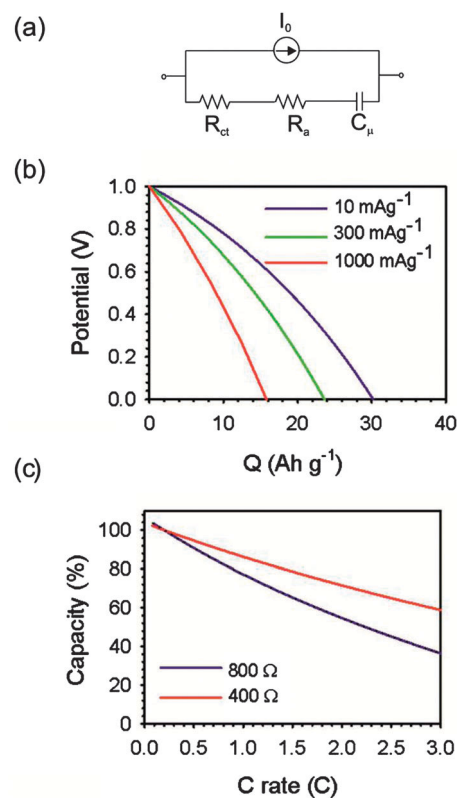

Fig. 6 (a) Simplified equivalent circuit used to model the voltage decay in the discharge experiment. I_0 is the extraction current, R_{ct} is the charge transfer resistance, R_a is the alloying resistance and C_μ is the chemical capacitance. (b) Voltage decay for different values of the specific current, I_0, is indicated in the inset panel. The charge transfer resistance was fixed at the value $R_{ct} = 800$ Ω. (c) Evolution of the capacity as a function of the current rate for two values of the charge transfer resistance (indicated in the inset panel of this figure).

Fig. 5 Fitting results using the equivalent circuit of Fig. 3(a) for the low-frequency circuit elements of Si and Si/Ge NT anodes showing (a) chemical capacitance C_μ and (b) alloying resistance R_a.

17934 | *Phys. Chem. Chem. Phys.*, 2014, **16**, 17930–17935

This journal is © the Owner Societies 2014

simulation is extracted for the time at which the potential attains zero. The potential drop at the resistive elements increases with the discharging current thus leaving non-extracted charge in the capacitor. The simulation roughly reproduces the voltage decay and capacity plots of Fig. 1c and d, as depicted by Fig. 6b and c. The detailed procedure of these simulations is given in the ESI.† As expected, higher specific current produces faster voltage fall, while larger charge transfer resistances are responsible for higher decrease in the capacity of the system. Doubling the resistance approximately reproduces the reduction in capacity observed in Fig. 1d at 3 C rate evaluation. Although the simulation is certainly an oversimplification of a real battery electrode, it highlights the role of resistive elements in the overall rate capability performance.

Conclusions

We have identified the mechanism that causes the difference in rate capability between Si NT and Si–Ge DLNT electrodes for Li-ion battery anodes. It is observed by impedance spectroscopy that the intake of Li-ions from the electrolyte into the active materials is highly favored by the Ge shell covering inner Si nanotubes. This is mainly related to the higher electronic conductivity that Ge possesses in comparison to Si. The total resistance for Si NT electrodes doubles that encountered for Si/Ge DLNT structures.

Conflicts of interest

The authors declare no competing financial interest.

Acknowledgements

References

1 T. Song, L. B. Hu and U. Paik, *J. Phys. Chem. Lett.*, 2014, **5**, 720–731.

2 U. Kasavajjula, C. S. Wang and A. J. Appleby, *J. Power Sources*, 2007, **163**, 1003–1039.

3 H. Wu and Y. Cui, *Nano Today*, 2012, **7**, 414–429.

4 J. R. Szczech and S. Jin, *Energy Environ. Sci.*, 2011, **4**, 56–72.

5 C. K. Chan, H. Peng, G. Liu, K. McIlwrath, X. F. Zhang, R. A. Huggins and Y. Cui, *Nat. Nanotechnol.*, 2008, **3**, 31–35.

6 Y. Xiao, D. Hao, H. Chen, Z. Gong and Y. Yang, *ACS Appl. Mater. Interfaces*, 2013, **5**, 1681–1687.

7 T. Song, J. L. Xia, J. H. Lee, D. H. Lee, M. S. Kwon, J. M. Choi, J. Wu, S. K. Doo, H. Chang, W. Il Park, D. S. Zang, H. Kim, Y. G. Huang, K. C. Hwang, J. A. Rogers and U. Paik, *Nano Lett.*, 2010, **10**, 1710–1716.

8 G. Kim, S. Jeong, J.-H. Shin, J. Cho and H. Lee, *ACS Nano*, 2014, **8**, 1907–1912.

9 G. Jeong, J.-G. Kim, M.-S. Park, M. Seo, S. M. Hwang, Y.-U. Kim, Y.-J. Kim, J. H. Kim and S. X. Dou, *ACS Nano*, 2014, **8**, 2977–2985.

10 Y. Chen, S. Zeng, J. Qian, Y. Wang, Y. Cao, H. Yang and X. Ai, *ACS Appl. Mater. Interfaces*, 2014, **6**, 3508–3514.

11 M. R. Jo, Y.-U. Heo, Y. C. Lee and Y.-M. Kang, *Nanoscale*, 2014, **6**, 1005–1010.

12 W.-S. Kim, Y. Hwa, J.-H. Shin, M. Yang, H.-J. Sohn and S.-H. Hong, *Nanoscale*, 2014, **6**, 4297–4302.

13 P. Wu, H. Wang, Y. Tang, Y. Zhou and T. Lu, *ACS Appl. Mater. Interfaces*, 2014, **6**, 3546–3552.

14 C. Yue, Y. Yu, Z. Wu, X. He, J. Wang, J. Li, C. Li, S. Wu, J. Li and J. Kang, *Nanoscale*, 2014, **6**, 1817–1822.

15 T. Song, H. Cheng, H. Choi, J.-H. Lee, H. Han, D. H. Lee, D. S. Yoo, M.-S. Kwon, J.-M. Choi, S. G. Doo, H. Chang, J. Xiao, Y. Huang, W. I. Park, Y.-C. Chung, H. Kim, J. A. Rogers and U. Paik, *ACS Nano*, 2012, **6**, 303–309.

16 T. Song, H. Cheng, K. Town, H. Park, R. W. Black, S. Lee, W. I. Park, Y. Huang, J. A. Rogers, L. F. Nazar and U. Paik, *Adv. Funct. Mater.*, 2014, **24**, 1458–1464.

17 Y. Yu, C. Yue, S. Sun, W. Lin, H. Su, B. Xu, J. Li, S. Wu, J. Li and J. Kang, *ACS Appl. Mater. Interfaces*, 2014, **6**, 5884–5890.

18 R. Hass, J. García-Cañadas and G. Garcia-Belmonte, *J. Electroanal. Chem.*, 2005, **577**, 99–105.

19 J. Bisquert, *Phys. Chem. Chem. Phys.*, 2003, **5**, 5360–5364.

20 J. Song and M. Z. Bazant, *J. Electrochem. Soc.*, 2013, **160**, A15–A24.

21 M. Levi and D. Aurbach, *J. Phys. Chem. B*, 2004, **108**, 11693–11703.

22 J. P. Meyers, M. Doyle, R. M. Darling and J. Newman, *J. Electrochem. Soc.*, 2000, **147**, 2930–2940.

23 C. Xu, Y. Zeng, X. Rui, J. Zhu, H. Tan, A. Guerrero, J. Toribio, J. Bisquert, G. Garcia-Belmonte and Q. Yan, *J. Phys. Chem. C*, 2013, **117**, 17462–17469.

24 F. Martinez-Julian, A. Guerrero, M. Haro, J. Bisquert, D. Bresser, E. Paillard, S. Passerini and G. Garcia-Belmonte, *J. Phys. Chem. C*, 2014, **118**, 6069–6076.

This journal is © the Owner Societies 2014

Phys. Chem. Chem. Phys., 2014, **16**, 17930–17935 | **17935**